Available online at www.sciencedirect.com
SCIENCE DIRECT®
Engineering Fracture Mechanics 72 (2005) 1635–1663
Engineering Fracture Mechanics
www.elsevier.com/locate/engfracmech

Interaction integral procedures for 3-D curved cracks including surface tractions

Matthew C. Walters, Glaucio H. Paulino, Robert H. Dodds Jr. *

Department of Civil and Environmental Engineering, University of Illinois at Urbana-Champaign, Newmark Civil Engineering Laboratory, 205 N. Mathews Avenue, Urbana, IL 61801, United States

Received 7 July 2004; received in revised form 6 December 2004; accepted 7 January 2005

Abstract

This study examines a two-state interaction integral for the direct computation of mixed-mode stress intensity factors along curved cracks under remote mechanical loads and applied crack-face tractions. We investigate the accuracy of stress intensity factors computed along planar, curved cracks in homogeneous materials using a simplified interaction integral that omits terms to reflect specifically the effects of local crack-front curvature. We examine the significance of the crack-face traction term in the interaction integral, and demonstrate the benefit of a simple, exact numerical integration procedure to evaluate the integral for one class of three-dimensional elements. The work also discusses two approaches to compute auxiliary, interaction integral quantities along cracks discretized by linear and curved elements. Comparisons of numerical results with analytical solutions for stress intensity factors verify the accuracy of the proposed interaction integral procedures.

Keywords: Interaction integral; Mixed-mode stress intensity factors; Crack-face traction; 3-D; Curved cracks

1. Introduction

The determination of accurate stress intensity factors for mixed-mode loading in complex, three-dimensional (3-D) configurations remains a significant challenge in computational fracture mechanics. Defect assessments of industrial structures require reliable estimates of stress intensity factors—especially for fatigue life predictions that adopt a damage tolerance philosophy. Finite element models of complex components must have sufficient refinement to resolve strong gradients in the near-tip fields along curved crack

* Corresponding author. Tel.: +1 217 333 3276; fax: +1 217 333 9464.
E-mail address: rdodds@uiuc.edu (R.H. Dodds).

0013-7944/$ - see front matter © 2005 Elsevier Ltd. All rights reserved.
doi:10.1016/j.engfracmech.2005.01.002

fronts and must be coupled with robust numerical methods to extract the mixed-mode stress intensity factors from the solutions pointwise along the front. Interaction integral methods have emerged as perhaps the most accurate and readily implementable approach to extract mixed-mode, stress intensity factors. These methods post-process the computed displacements, strains and stresses from the finite element model that are taken to represent the correct equilibrium state for the specified boundary-value problem. Another selected equilibrium state supplies auxiliary near-tip fields defined in terms of the mixed-mode stress intensity factors. For this purpose, Williams' solution [1] for the two-dimensional (2-D) asymptotic stress and displacement fields in the vicinity of a crack represents a widely-used auxiliary field. A linear combination of finite element fields (commonly termed the "actual" fields) with auxiliary fields constitutes a third, superimposed, equilibrium state. One class of interaction integrals arises from an interpretation of the J-integral [2]—the computation of J for the superimposed state leads to a conservation integral composed of interacting actual and auxiliary terms that permits direct computation of stress intensity factors [3]. Numerical evaluation of this interaction integral fits conveniently into existing domain-integral procedures for J-computation [4], thereby providing a readily implemented, robust and accurate tool for linear-elastic analyses.

Through post-processing of finite-element results, Yau et al. [5] evaluate an interaction integral to determine mixed-mode stress intensity factors for 2-D cracks in specimens under mechanical loading. Studies of interaction integral procedures for 3-D cracks include analyses of plates under in-plane loading [6] and elastic–plastic interface cracks [7]. Dhondt [8] examines the variation in crack front singularity along quarter-circular corner cracks. Krysl and Belytschko [9] employ the element free Galerkin method to analyze the dynamic propagation of arbitrary 3-D cracks in homogeneous material. Most prior works provide interaction integral solutions for cracks with traction-free faces in homogeneous or bi-material specimens under quasi-static, isothermal loading. Nakamura and Parks [10] discuss the formulation of an interaction integral for thermal and body-force loads, and Cho et al. [11] analyze 2-D interface cracks with surface tractions that interact with additional singularities caused by point forces or dislocations. Other interaction integrals follow from the application of Betti's reciprocal work theorem [12], or the M- and L-integrals of Knowles and Sternberg [13–15]. Kim et al. [16] compute stress intensity factors along curved cracks in homogeneous 3-D solids using an interaction integral derived from the M-integral [13].

This study examines a J-integral based, interaction integral procedure to compute mixed-mode stress intensity factors for curved, planar cracks in three-dimensional homogeneous solids under remote mechanical loading and/or applied crack-face tractions. For cracked, axisymmetric configurations and for curved 3-D cracks, the 2-D Williams solutions [1] do not satisfy equilibrium or strain–displacement compatibility when expressed in curvilinear coordinates, thereby leading to additional terms in the interaction integral [17]. Nahta and Moran [17] include these curvature effects to study axisymmetric interface cracks. They suggest that inclusion of the curvature effects generally should improve the interaction integral values for a particular level of mesh refinement. Gosz et al. [18] and Gosz and Moran [19] also include the effects of local crack front curvature to analyze 3-D curved interface cracks and non-planar 3-D cracks, respectively. They note the potential for significant error if the crack-front curvature terms are neglected. The present work investigates to what extent mesh refinement may reduce this observed error in interaction integral computations that do not include the recommended curvature terms. The present treatment addresses curved, planar 3-D cracks in homogeneous material. We compare values from this simplified interaction integral with J-integral values and with analytical stress intensity factor solutions using finite-element models that have reasonable levels of mesh refinement in the crack-front region. These comparisons illustrate the good accuracy that can be obtained using the standard 3-D interaction integral for straight cracks, which has the advantage of being much simpler to implement than the full expression that includes curvature terms. Curvature of crack surfaces imposes additional considerations on the interaction integral [19] which are not discussed here. Also, interaction integrals studied in this work do not capture the change in singular fields near the intersection of a crack with a free surface. See Im and Kim [14], and Lee and Im [20] for interaction integral treatments of this case.

Shih et al. [4] describe a domain integral procedure to evaluate the *J*-integral along a 3-D crack front that incorporates a surface integral over traction-bearing crack faces (needed to maintain path independence). A crack-face integral also becomes necessary to preserve path independence of the interaction integral method. Cho et al. [11] employ such an integral in their study of cracks with surface tractions in 2-D bodies. Gosz and Moran [19] integrate over crack surfaces to compute stress intensity factors for traction-free, non-planar cracks. The necessary surface integral, however, does not appear in some other interaction integral treatments of traction-bearing cracks. This study examines the importance of the crack-face integral and presents a simple, exact integration procedure applicable for one class of 3-D finite elements.

The plan of this paper is as follows: Section 2 reviews the domain-integral technique that forms the basis of current numerical procedures. Section 3 discusses the interaction integral procedure to compute mixed-mode stress intensity factors along curved 3-D cracks in homogeneous solids under quasi-static, mechanical loads including applied crack-face tractions. A description of numerical procedures follows in Section 4. Section 5 describes a 3-D analysis of a 2-D plane-strain problem that provides insight into the influence of the crack-face traction integral and the improvement offered by its exact integration. Section 6 presents mixed-mode stress intensity factors computed using the interaction integral without curvature terms, and compares them to values obtained from analytical solutions. Some observations conclude the work in Section 8.

2. A domain integral for 3-D cracks with surface tractions

Shih et al. [4] develop the domain-integral method as a powerful numerical procedure to evaluate the *J*-integral for 3-D cracks. The domain-based, interaction integral methods build upon this approach. An expression for the *J*-integral at location s along a 3-D crack front is [4]

$$J(s) = \lim_{\Gamma \to 0} \int_{\Gamma} (W\delta_{1i} - \sigma_{ij}u_{j,1})n_i \mathrm{d}\Gamma, \tag{1}$$

where W is strain energy density, σ_{ij} represents stress components, u_j denotes displacement components, and δ_{ij} is the Kronecker delta. Latin subscripts range from 1 to 3, and unless noted otherwise, repeated indices imply summation. The partial derivative $(\cdot)_{,i} = \partial(\cdot)/\partial X_i$ indicates the spatial derivative of $(\cdot)$ with respect to direction X_i of the local coordinate system defined at crack front position s as shown in Fig. 1. The contour, Γ, with normal-vector components n_i, lies in the X_1–X_2 plane of the local coordinate system, and extends from the bottom crack-face to the top crack-face. When the contour shrinks to the crack front at s,

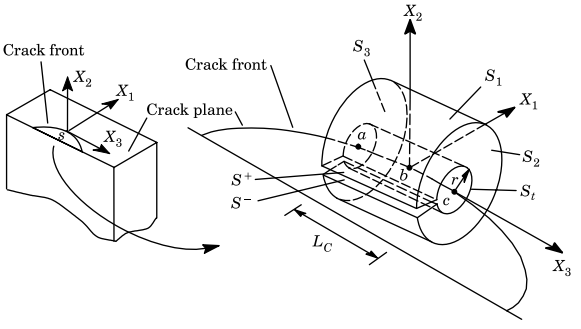

Fig. 1. Domains used to compute area and volume integrals at crack-front location $s = b$, extend over length L_c from point a to point c. Surfaces S_t and S_1 (cylindrical surfaces), S_2 and S_3 (flat lateral surfaces), and S^+, and S^- (top and bottom crack-face surfaces) comprise surface S and enclose volume V. For general loading conditions, S_t must shrink to the crack front, i.e. $r \to 0^+$.

Eq. (1) equals Rice's J-integral [2] and remains valid in the presence of general material behavior, body forces, crack-face tractions and thermal strains.

Shih et al. [4] transform Eq. (1) into volume and surface integrals suitable for numerical evaluation in a 3-D finite-element context. They derive an expression for $\overline{J}(s)$, the energy released per unit advance of crack front segment L_c (see Fig. 1). This expression may be written as

$$\overline{J}(s) = \int_V (\sigma_{ij}u_{j,1} - W\delta_{1i})q_{,i}\,\mathrm{d}V + \int_V (\sigma_{ij}u_{j,1} - W\delta_{1i})_{,i}q\,\mathrm{d}V - \int_{S^+ + S^-} t_j u_{j,1} q\,\mathrm{d}S, \tag{2}$$

where t_j are components of traction acting on the crack-face. Here, surfaces S^+, S^-, S_1, S_t, S_2 and S_3 shown in Fig. 1, enclose the simply-connected volume V, and surface S_t shrinks to the crack front (i.e. $r \to 0$). The scalar weight-function, q, varies smoothly within V. A simple form for q assigns it a smooth variation from zero on surfaces S_1, S_2 and S_3 to a value of 1.0 at location s on S_t [4].

For elastic, homogeneous materials under quasi-static, isothermal loading with no body forces or crack-face tractions, the second and third integrals in Eq. (2) vanish. For curved cracks, the second integral in Eq. (2) does not vanish. Eq. (2) assumes that crack-front curvature within the domain of integration is negligible, and is not strictly valid for cracks with curved surfaces or curved crack fronts. Fernlund et al. [21] and Eriksson [22] develop expressions to evaluate the J-integral and crack-extension force along curved, non-planar 3-D cracks using curvilinear coordinates. The third integral in Eq. (2) reflects the contribution of applied crack-face tractions. Shih et al. [4] assume that the energy release rate varies slowly along crack-segment L_c, and thus obtain the approximate expression

$$J(s) = \frac{\overline{J}(s)}{\int_{L_c} q(s)\mathrm{d}s}, \tag{3}$$

for the energy release rate, $J(s)$, at location s along a 3-D crack front.

3. An interaction integral procedure for curved 3-D cracks with surface tractions

This section reviews the formulation of an interaction integral for isothermal, quasi-static loading of planar, 3-D curved cracks in homogeneous materials under remote loads and crack-face tractions. We discuss a formulation that includes the effects of crack front curvature, and then describe the computational procedure to obtain stress intensity factors.

3.1. Auxiliary fields

Williams' solution [1] for auxiliary stress and displacement in the vicinity of a crack has the form:

$$\sigma_{ij}^{\mathrm{aux}} = \frac{K_{\mathrm{I}}^{\mathrm{aux}}}{\sqrt{2\pi r}} f_{ij}^{\mathrm{I}}(\theta) + \frac{K_{\mathrm{II}}^{\mathrm{aux}}}{\sqrt{2\pi r}} f_{ij}^{\mathrm{II}}(\theta) + \frac{K_{\mathrm{III}}^{\mathrm{aux}}}{\sqrt{2\pi r}} f_{ij}^{\mathrm{III}}(\theta), \tag{4}$$

$$u_j^{\mathrm{aux}} = \frac{K_{\mathrm{I}}^{\mathrm{aux}}}{2\mu}\sqrt{\frac{r}{2\pi}} g_j^{\mathrm{I}}(\theta, v) + \frac{K_{\mathrm{II}}^{\mathrm{aux}}}{2\mu}\sqrt{\frac{r}{2\pi}} g_j^{\mathrm{II}}(\theta, v) + \frac{2K_{\mathrm{III}}^{\mathrm{aux}}}{\mu}\sqrt{\frac{r}{2\pi}} g_j^{\mathrm{III}}(\theta, v), \tag{5}$$

where superscript "aux" denotes auxiliary fields. Appendix A provides the expressions for $f_{ij}(\theta)$ as well as the plane-stress and plane-strain forms for $g_j(\theta, v)$. The symmetric gradient of displacements defines the auxiliary strain components:

$$\varepsilon_{ij}^{\mathrm{aux}} = \frac{1}{2}\left(u_{i,j}^{\mathrm{aux}} + u_{j,i}^{\mathrm{aux}}\right). \tag{6}$$

These 2-D auxiliary fields are a function of location r and θ, and shear modulus μ. Most interaction integral studies use the plane-strain form of these auxiliary fields to analyze cracks in 3-D solids, with the assumption that plane-strain conditions exist (asymptotically) near the crack front at locations away from free surfaces. The excellent accuracy (<1%) of reported stress intensity factors supports the adequacy of this approximation. In an alternative approach, Kim et al. [16] demonstrate the use of numerically-generated auxiliary fields to obtain stress intensity factors.

Nahta and Moran [17], Gosz et al. [18] and Gosz and Moran [19] develop interaction integral procedures that use the 2-D auxiliary fields based on Eqs. (4)–(6) for axisymmetric interface cracks, curved 3-D interface cracks, and 3-D cracks with non-planar surfaces, respectively. In a finite-element context, values of r and θ in these expressions describe the position of an element integration point in curvilinear coordinates, relative to a curved crack front. Definition of the auxiliary fields in curvilinear coordinates gives rise to additional terms in the gradients of auxiliary displacements [17–19]. To quantify the accuracy of interaction integral computations without terms for crack curvature, numerical studies here use curvilinear coordinates to compute r and θ for auxiliary fields, but omit these additional, auxiliary-field gradients during evaluation of the interaction integral.

3.2. Interaction integral formulation

By superimposing actual (computed) equilibrium fields and auxiliary fields, $\overline{J}(s)$ for the superimposed state, $\overline{J}^{\mathrm{S}}$, from Eq. (2) becomes

$$\overline{J}^{\mathrm{S}}(s) = \int_V \left[(\sigma_{ij}+\sigma_{ij}^{\mathrm{aux}})(u_{j,1}+u_{j,1}^{\mathrm{aux}}) - W^{\mathrm{S}}\delta_{1i}\right] q_{,i}\,\mathrm{d}V + \int_V \left[(\sigma_{ij}+\sigma_{ij}^{\mathrm{aux}})(u_{j,1}+u_{j,1}^{\mathrm{aux}}) - W^{\mathrm{S}}\delta_{1i}\right]_{,i} q\,\mathrm{d}V - \int_{S^+ + S^-} (t_j + t_j^{\mathrm{aux}})(u_{j,1}+u_{j,1}^{\mathrm{aux}}) q\,\mathrm{d}S. \tag{7}$$

Here, superscript 'S' denotes the superimposed state. For a linear-elastic material, the strain energy density for the superimposed state, W^{S}, is

$$W^{\mathrm{S}} = \frac{1}{2}(\sigma_{ij}+\sigma_{ij}^{\mathrm{aux}})(\varepsilon_{ij}+\varepsilon_{ij}^{\mathrm{aux}}) = W + W^{\mathrm{aux}} + W^{\mathrm{I}}, \tag{8}$$

where W^{I} is

$$W^{\mathrm{I}} = \frac{1}{2}\left(\sigma_{ij}\varepsilon_{ij}^{\mathrm{aux}} + \sigma_{ij}^{\mathrm{aux}}\varepsilon_{ij}\right). \tag{9}$$

With Eq. (8), $\overline{J}^{\mathrm{S}}$ separates into three parts

$$\overline{J}^{\mathrm{S}}s = \overline{J}(s) + \overline{J}^{\mathrm{aux}}(s) + \overline{I}(s), \tag{10}$$

where $\overline{J}(s)$ equals Eq. (2), the domain integral for the actual state; $\overline{J}^{\mathrm{aux}}(s)$ is the domain integral for the auxiliary state; and $\overline{I}(s)$ is an integral with interacting actual and auxiliary terms, written as

$$\overline{I}^{\mathrm{S}}(s) = \int_V \left[\sigma_{ij}u_{j,1}^{\mathrm{aux}} + \sigma_{ij}^{\mathrm{aux}}u_{j,1} - \frac{1}{2}\left(\sigma_{jk}\varepsilon_{jk}^{\mathrm{aux}} + \sigma_{jk}^{\mathrm{aux}}\varepsilon_{jk}\right)\delta_{1i}\right] q_{,i}\,\mathrm{d}V + \int_V \left[\sigma_{ij}u_{j,1}^{\mathrm{aux}} + \sigma_{ij}^{\mathrm{aux}}u_{j,1} - \frac{1}{2}\left(\sigma_{jk}\varepsilon_{jk}^{\mathrm{aux}} + \sigma_{jk}^{\mathrm{aux}}\varepsilon_{jk}\right)\delta_{1i}\right]_{,i} q\,\mathrm{d}V - \int_{S^+ + S^-} \left(t_j u_{j,1}^{\mathrm{aux}} + t_j^{\mathrm{aux}}u_{j,1}\right) q\,\mathrm{d}S. \tag{11}$$

The third integral of Eq. (11) vanishes for crack-faces without applied tractions. For straight cracks, the second integral vanishes for quasi-static, isothermal loading of homogeneous materials in the absence of body forces. Auxiliary fields based on Williams' 2-D solution do not satisfy equilibrium or compatibility in curvilinear coordinates [17], however, and the second integral remains non-zero for curved cracks.

The interaction integral procedure here assumes that the same constitutive tensor, C_{ijkl}, couples actual and auxiliary stress and strain components, i.e.

$$\sigma_{ij} = C_{ijkl}\varepsilon_{kl} \quad \text{and} \quad \sigma_{ij}^{\text{aux}} = C_{ijkl}\varepsilon_{kl}^{\text{aux}}. \tag{12}$$

With appropriate definitions of auxiliary strain components, the constitutive tensor is the same for the 3-D actual fields and for the 2-D auxiliary fields. Eq. (12) leads to the useful relationships

$$\sigma_{ij}\varepsilon_{ij}^{\text{aux}} = C_{ijkl}\varepsilon_{kl}\varepsilon_{ij}^{\text{aux}} = C_{klij}\varepsilon_{ij}^{\text{aux}}\varepsilon_{kl} = \sigma_{ij}^{\text{aux}}\varepsilon_{ij}, \tag{13}$$

which enable simplification of the stress–strain terms in the first and second integrals of Eq. (11). Expansion of the second integral in Eq. (11) simplifies because $\sigma_{ij,i}u_{j,1}^{\text{aux}} \equiv 0$ due to equilibrium of the actual stresses, and Eq. (13) leads to the cancellation of two additional terms

$$\begin{aligned}\sigma_{ij}^{\text{aux}}u_{j,1i} - \sigma_{ij,1}\varepsilon_{ij}^{\text{aux}} &= \sigma_{ij}^{\text{aux}}u_{j,1i} - C_{ijkl,1}\varepsilon_{kl}\varepsilon_{ij}^{\text{aux}} + C_{ijkl}\varepsilon_{kl,1}\varepsilon_{ij}^{\text{aux}} = \sigma_{ij}^{\text{aux}}u_{j,1i} - C_{klij}\varepsilon_{ij}^{\text{aux}}\varepsilon_{kl,1} \\ &= \sigma_{ij}^{\text{aux}}u_{j,1i} - \sigma_{ij}^{\text{aux}}\varepsilon_{ij,1} = 0.\end{aligned} \tag{14}$$

Nahta and Moran [17] observe that 2-D plane-strain auxiliary fields based on Williams' solution do not satisfy strain–displacement compatibility and equilibrium when defined in curvilinear coordinates. Therefore

$$\sigma_{ij}(u_{j,1i}^{\text{aux}} - \varepsilon_{ij,1}^{\text{aux}}) \neq 0 \quad \text{and} \quad \sigma_{ij,i}^{\text{aux}} \neq 0. \tag{15}$$

Because auxiliary fields correspond to an arbitrarily-specified equilibrium state, the third integral in Eq. (11) simplifies with the assumption that the auxiliary state has crack-faces without applied tractions. As a result of the preceding arguments, Eq. (11) reduces to

$$\begin{aligned}\overline{I}(s) = &\int_V \left(\sigma_{ij}u_{j,1}^{\text{aux}} + \sigma_{ij}^{\text{aux}}u_{j,1} - \sigma_{jk}\varepsilon_{jk}^{\text{aux}}\delta_{1i}\right)q_{,i}\,\mathrm{d}V + \int_V \left[\sigma_{ij}\left(u_{j,1i}^{\text{aux}} - \varepsilon_{ij,1}^{\text{aux}}\right) + \sigma_{ij,1}^{\text{aux}}u_{j,1}\right]q\,\mathrm{d}V \\ &- \int_{S^+ + S^-} t_j u_{j,1}^{\text{aux}} q\,\mathrm{d}S.\end{aligned} \tag{16}$$

The terms $\sigma_{ij}(u_{j,1i}^{\text{aux}} - \varepsilon_{ij,1}^{\text{aux}})$ and $\sigma_{ij,i}^{\text{aux}}u_{j,1}$ that arise here due to crack front curvature also appear in the interaction integral formulations for straight cracks in functionally-graded materials [23,24]. For straight cracks in homogeneous material, the second integral of Eq. (16) vanishes. The crack-face integral,

$$\int_{S^+ + S^-} t_j u_{j,1}^{\text{aux}} q\,\mathrm{d}S, \tag{17}$$

contributes significantly to stress intensity factors, but is occasionally neglected in the literature. None of the quantities in Eq. (17) depend upon the finite element solution of the boundary-value problem—an exact evaluation of this integral thus ensures that it does not contribute error to numerical results. Section 4.3 and Appendix C describe a simple, exact numerical integration procedure for Eq. (17) when element edges along the crack front are straight.

With the value of $\overline{I}(s)$ generated using Eq. (16), computation of a pointwise value of the interaction integral at location s, along a 3-D crack front follows Eq. (3):

$$I(s) = \frac{\overline{I}(s)}{\int_{L_c} q(s)\,\mathrm{d}s}. \tag{18}$$

3.3. Extraction of stress intensity factors

An expression for the energy release rate in terms of mixed-mode stress intensity factors K_{I}, K_{II} and K_{III} is [25]

$$J(s) = \frac{K_{\mathrm{I}}^2 + K_{\mathrm{II}}^2}{E^*} + \frac{1+v}{E} K_{\mathrm{III}}^2, \tag{19}$$

which assumes self-similar crack growth. As usual, $E^* = E/(1-v^2)$ for plane-strain, $E^* = E$ for plane-stress conditions, and stress intensity factors refer to crack front location s. For the superimposed state, Eq. (19) becomes

$$\begin{aligned} J^{\mathrm{S}}(s) &= \frac{1}{E^*}\left[(K_{\mathrm{I}} + K_{\mathrm{I}}^{\mathrm{aux}})^2 + (K_{\mathrm{II}} + K_{\mathrm{II}}^{\mathrm{aux}})^2\right] + \frac{1+v}{E}(K_{\mathrm{III}} + K_{\mathrm{III}}^{\mathrm{aux}})^2, \\ &= J(s) + J^{\mathrm{aux}}(s) + I(s), \end{aligned}$$

where

$$I(s) = \frac{1}{E^*}\left(2K_{\mathrm{I}}K_{\mathrm{I}}^{\mathrm{aux}} + 2K_{\mathrm{II}}K_{\mathrm{II}}^{\mathrm{aux}}\right) + \frac{1+v}{E}\left(2K_{\mathrm{III}}K_{\mathrm{III}}^{\mathrm{aux}}\right). \tag{20}$$

Eqs. (18) and (20) provide the sought-after relationship between stress intensity factors and the interaction integral in Eq. (16). With the assigned values $K_{\mathrm{I}}^{\mathrm{aux}} = 1.0$ and $K_{\mathrm{II}}^{\mathrm{aux}} = K_{\mathrm{III}}^{\mathrm{aux}} = 0$, Eq. (20) yields

$$K_{\mathrm{I}} = \frac{E^*}{2} I(s). \tag{21}$$

To obtain the actual mode-I stress intensity factor from (21), we: (1) assume either plane-stress or plane-strain conditions for E^* and for the auxiliary fields; (2) compute $\overline{I}(s)$ by evaluating the interaction integral in Eq. (16) using the values $K_{\mathrm{I}}^{\mathrm{aux}} = 1.0$, $K_{\mathrm{II}}^{\mathrm{aux}} = 0.0$, and $K_{\mathrm{III}}^{\mathrm{aux}} = 0$; (3) compute $I(s)$ from Eq.(18) for use in Eq. (21).

The selection $K_{\mathrm{II}}^{\mathrm{aux}} = 1.0$, $K_{\mathrm{I}}^{\mathrm{aux}} = K_{\mathrm{III}}^{\mathrm{aux}} = 0$, and the selection $K_{\mathrm{III}}^{\mathrm{aux}} = 1.0$, $K_{\mathrm{I}}^{\mathrm{aux}} = K_{\mathrm{II}}^{\mathrm{aux}} = 0$ in Eq. (20) leads to relationships between K_{II} , K_{III} and $I(s)$:

$$K_{\mathrm{II}} = \frac{E^*}{2} I(s), \text{ and } K_{\mathrm{III}} = \mu I(s). \tag{22}$$

To obtain values of K_{II} and K_{III} from Eq. (22), we evaluate Eqs. (16), (18) and (22) with appropriate values of $K_{\mathrm{I}}^{\mathrm{aux}}$, $K_{\mathrm{II}}^{\mathrm{aux}}$, and $K_{\mathrm{III}}^{\mathrm{aux}}$. Five distinct evaluations of the interaction integral in Eq. (16) thus lead to values of K_{I} and K_{II} for plane-stress and plane-strain conditions, and to a value of K_{III} for anti-plane-shear conditions. Section 4 discusses the numerical evaluation of Eq. (16).

4. Numerical procedures

Within a finite-element framework, numerical procedures to evaluate the interaction integral parallel those used in conventional, element-level computations. This section describes numerical evaluation of the integrals, discusses computation of r and θ for the auxiliary-fields and reviews procedures to evaluate the surface-traction integral in Eq. (17). All procedures employed in this work are implemented in WARP3D, a general purpose, open source finite element code [26].

4.1. Numerical evaluation of volume and surface integrals

Evaluation of the integrals in Eq. (16) follows the same Gauss-quadrature procedures employed for the computation of element stiffnesses [27]:

$$\begin{aligned} \overline{I}(s) = &\sum_{V}^{\mathrm{elems}} \sum_{p}^{\mathrm{gpts}} \left[\left(\sigma_{ij} u_{j,1}^{\mathrm{aux}} + \sigma_{ij}^{\mathrm{aux}} u_{j,1} - \sigma_{jk}\varepsilon_{jk}^{\mathrm{aux}}\delta_{1i}\right) q_{,i} \det \mathbf{J}\right]_p w_p \\ &+ \sum_{V}^{\mathrm{elems}} \sum_{p}^{\mathrm{gpts}} \left\{\left[\sigma_{ij}\left(u_{j,1i}^{\mathrm{aux}} - \varepsilon_{ij,1}^{\mathrm{aux}}\right) + \sigma_{ij,i}^{\mathrm{aux}} u_{j,1}\right] q \det \mathbf{J}\right\}_p w_p - \sum_{S}^{\mathit{faces}} \sum_{p}^{\mathrm{gpts}} (t_j u_{j,1}^{\mathrm{aux}} q \det \mathbf{J})_p w_p, \end{aligned} \tag{23}$$

where the sum over volume V includes all elements in the domain, and the sum over surface S includes each traction-bearing element face on the boundary of domain V which lies on the crack surface. The sum over p includes all integration points, and w_p denotes the corresponding weight for that point. All quantities included in the summation must be expressed in the local, orthogonal coordinate system at location s on the crack front (see Fig. 1). Here, det **J** denotes the determinant of the coordinate Jacobian matrix in two or three dimensions, depending upon surface or volume domains. Repeated indices imply summation. We employ a simple "plateau" function for the variation of q [4], and Gauss quadrature based on the two-point rule for linear- and quadratic-displacement elements.

4.2. Computation of r and θ for auxiliary fields

Evaluation of the auxiliary fields at an integration point requires the distance r from the crack front to the point, and the angle, θ, measured from the crack-plane ahead of the crack to the integration point (see Fig. 2). For curved crack fronts, Gosz et al. [18] define the distance r between an integration point and the analytically-defined crack front using a curvilinear coordinate system. They first project an integration point, P, onto the crack plane as point C in Fig. 2(a), and then formulate an expression for the distance between C and the analytical definition of the curved crack front. Minimization of this distance through a Newton procedure determines the point E along the analytically-defined crack front closest to C (see Fig. 2(a)). Distance r is finally measured from E to P, and angle P–E–C determines θ.

The present work considers two different approaches to compute r and θ. For curved crack fronts discretized using quadratic elements with curved edges, i.e. elements with nodes that lie on the analytically-defined curve, computation of r and θ follows the above procedure employed by Gosz et al. [18], in which

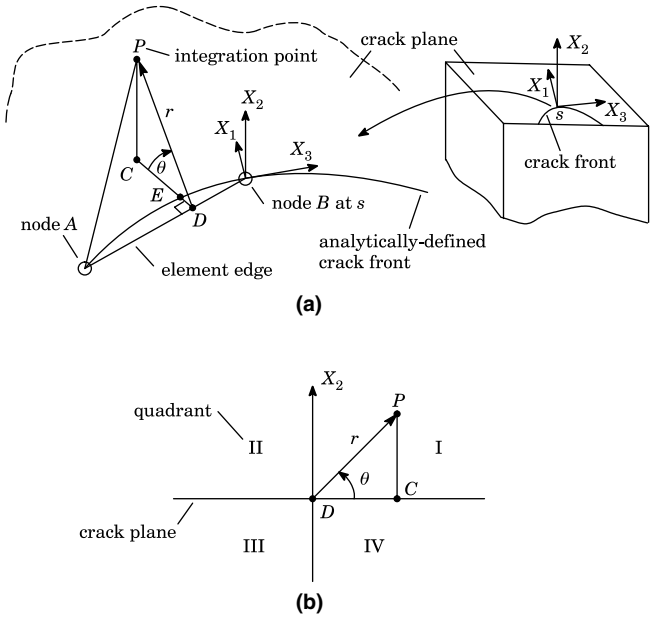

Fig. 2. (a) Computation of r and θ values to determine auxiliary fields at integration point P for interaction integral evaluation at crack-front location s. In meshes with straight element edges, distance r spans point P and the element edge between nodes A and B, and angle PDC defines θ. Point C is the projection of P onto the X_1–X_3 plane. (b) Quadrants I–IV in the plane PDC for computation of θ.

case angle P–E–C equals angle P–D–C because location E coincides with location D. For curved crack fronts discretized with linear elements (straight edges), r is the distance D–P from line segment A–B defined by element nodes, to integration point P, as illustrated in Fig. 2(a), and angle P–D–C determines θ. Figs. 2(a) and (b) and Appendix B describe a procedure to compute r and θ for this case. For a curved crack represented by straight-edged elements, this approach to define r and θ remains consistent with the discretization of the body into finite elements. It also avoids inaccurate computation of r and θ when the distance from the analytically-defined crack front to the mesh-defined crack front, distance D–E in Fig. 2(a), becomes significant compared to the width of elements in the domain of integration. Fig. 3(a) shows one quarter of a cylindrical mesh for an embedded penny-shaped crack discretized by elements with straight edges. Fig. 3(b) illustrates the potentially significant deviation of an analytical curve that describes a circular crack from the crack front defined by the mesh elements. The (actual) analytical curve in Fig. 3(b) extends into the fourth ring of elements surrounding the crack front, and does not correspond to the discontinuity in the mesh that defines the crack. Within the first few rings of elements that surround the crack front, r and θ values computed from the analytical curve locate incorrectly the position of integration points, thereby leading to auxiliary-fields inconsistent with actual fields generated by the mesh. This necessitates the use of local orthogonal coordinates to compute values of r and θ when elements with straight edges define the crack front. Numerical examples considered in this study employ finite-element meshes with curved crack fronts discretized using both straight and curved element edges.

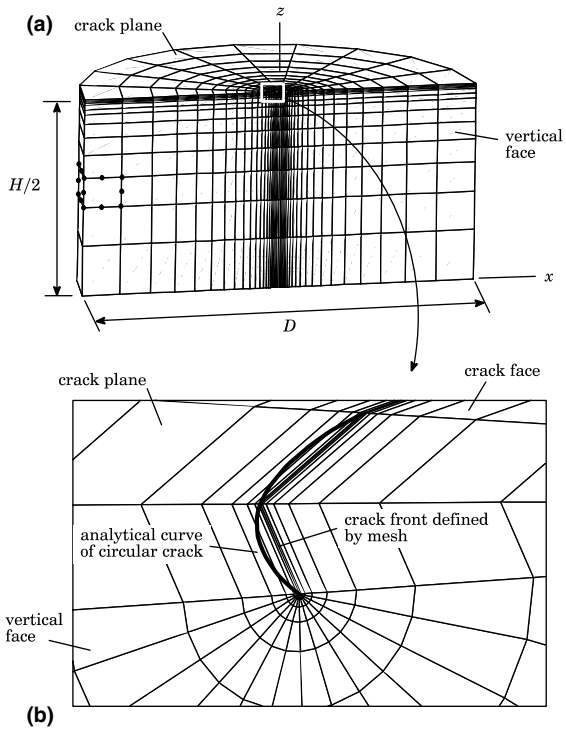

Fig. 3. (a) Quarter section of a circular cylindrical mesh with an embedded penny-shaped crack used for some examples in Section 7. (b) View of crack front discretized by elements with straight edges, showing difference between crack front defined by the mesh and by an analytical expression.

Table 1
Integration schemes used in this study to evaluate the crack-face-traction integral in Eq. (17)

Hexagonal-element geometry	Number of nodes on element face	Integration for face of element incident on crack	Integration for faces of elements remote from crack
Straight edges	4	Modified 2×2 (exact)	Standard 2×2
	8	Modified 2×2 (exact)	Standard 2×2
	8 (with quarter-point nodes)	Standard 2×2 (exact)	Standard 2×2
Curved edges	8 (with quarter-point nodes)	Standard 4×4	Standard 4×4

4.3. Numerical evaluation of the crack-surface-traction integral, Eq. (17)

Consider now integration of the surface-traction integral in Eq. (16) over the surface of an element incident on the crack front. Values of $K_{\mathrm{I}}^{\mathrm{aux}} = 1.0$, and $t_2 = 1.0$ correspond to a mode-I crack-opening surface pressure, and lead to an integrable, inverse square-root singularity:

$$\lim_{r\to0}\int_S t_j u_{j,1}^{\mathrm{aux}} q\,\mathrm{d}S = \lim_{r\to0}\int_0^Z\int_{x=0}^{x=r} \pm\frac{\mu}{\sqrt{x}}\mathrm{d}x\,\mathrm{d}z \approx \lim_{r\to0}\mathrm{O}(r^{1/2}) = 0, \tag{24}$$

where $q = 1.0$ for simplicity, and where the sign of the integrand depends upon the sign of $u_{j,1}^{\mathrm{aux}}$ at $\theta = \pm\pi$. The terms in Eq. (17) have no dependence on the solution to the boundary-value problem—crack-face tractions, auxiliary-displacement derivatives, q-values and the domain of integration are defined entirely by the analyst. During numerical evaluation, as the number of integration points increases, standard Gauss quadrature converges slowly toward the exact value for a function with a singularity at one end point [28]. A simple change of variables, detailed in Appendix C, leads to exact integration of Eq. (17) for elements with straight edges incident on the crack front, and requires only minor modifications to the standard Gauss-quadrature procedure. The modified Gauss integration, based on a 2×2 rule, leads to exact values of Eq. (17) for elements with four and eight nodes on each face. For quadratic elements with quarter-point nodes and straight edges, standard 2×2 Gauss quadrature integrates Eq. (17) exactly, and the change of variables becomes unnecessary. The exact integration procedure described in Appendix C is used here only for linear elements with loaded faces and incident on the crack front—standard 2×2 quadrature yields accurate values for elements with loaded faces not incident on the crack front. Standard quadrature, based on a four-point rule is adopted to evaluate Eq. (17) for elements with curved edges. Table 1 summarizes the various integration schemes used to evaluate Eq. (17). Numerical results presented here demonstrate that exact evaluation of Eq. (17) over elements incident on the crack front increases noticeably the accuracy of stress intensity factors.

5. 3-D analyses of plane-strain and plane-stress configurations

This section discusses verification of the 3-D numerical procedures to evaluate Eq. (16) for through-crack configurations with straight crack fronts. Finite element solutions for a standard boundary-layer model [29] (details omitted for brevity) verify the correct computation of mixed-mode stress intensity factors in homogeneous materials under plane-stress, plane-strain and anti-plane-shear conditions. The present finite element procedures yield the identical K_{I}, K_{II} and K_{III} values imposed on the remote boundary of the model. Here, we focus on the analysis of a single-edge-notch tension, SE(T), specimen under plane-strain conditions to illustrate the influence of the crack-face traction integral, Eq. (17).

Fig. 4(a) illustrates a semi-infinite strip subjected to crack-face tractions. Symmetry permits the analysis of one-half of the specimen. The finite-element mesh shown in Fig. 4(b) discretizes the model with 8-noded

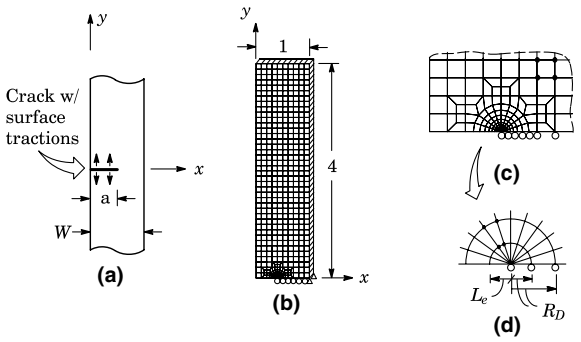

Fig. 4. (a) Schematic of a SE(T) specimen with crack-face tractions. (b) Symmetric mesh representing the cracked strip where $a/W = 0.4$. (c) Detail of mesh in crack-front region showing 10 semi-circular rings and 10 sectors of elements. (d) Elements incident on the crack front each have one collapsed face. Here, L_e describes the size of elements incident on the crack front, and R_D indicates domain size.

brick elements. Ten rings of elements surround the crack front, and 10 sectors of elements discretize the crack-front region in the hoop direction as shown in Fig. 4(c). Fig. 4(d) shows the collapsed elements incident on the crack front; L_e describes the size of elements incident on the crack front, and R_D describes the size of domains. For the domain of integration comprising the 10 elements immediately surrounding the crack front in the current model, only one element of size $L_e/a = 0.0177$ contributes to Eq. (17). With a 2×2 Gauss-quadrature rule, the ratio of numerical and exact values obtained from Eq. (17) for this element reflects an error greater than 25%. Fig. 5 illustrates the very slow convergence of standard quadrature toward the exact value of Eq. (17) with an increase in the number of quadrature points.

Fig. 6(a) shows the contribution to $\overline{I}(s)$ from each term in Eq. (16); recall that the second integral vanishes for a straight crack front. The error introduced by using standard 2×2 quadrature to evaluate Eq. (17) for the element incident on the crack front remains significant for large domains, as shown in Fig. 6(b). Current results obtained using "standard" quadrature match closely the stress intensity factor values obtained from ABAQUS 6.3 [31], also shown in Fig. 6(b). This figure shows that by following the procedure in Appendix C to evaluate Eq. (17) exactly over the element incident on the crack front, the accuracy of the stress intensity factor improves by about 1% from the solution obtained from standard 2×2

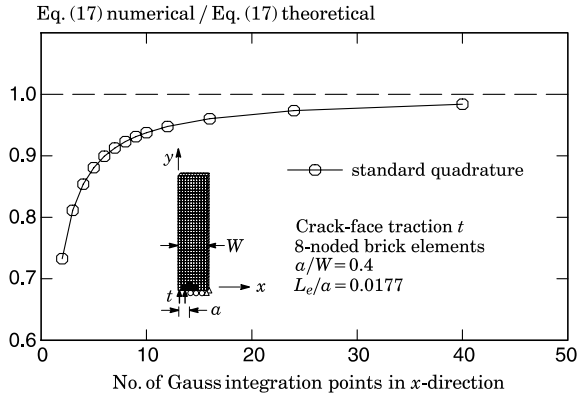

Fig. 5. Convergence of standard Gauss quadrature for evaluation of the crack-face traction integral, Eq. (17), for the element incident on the crack front in the SE(T) model.

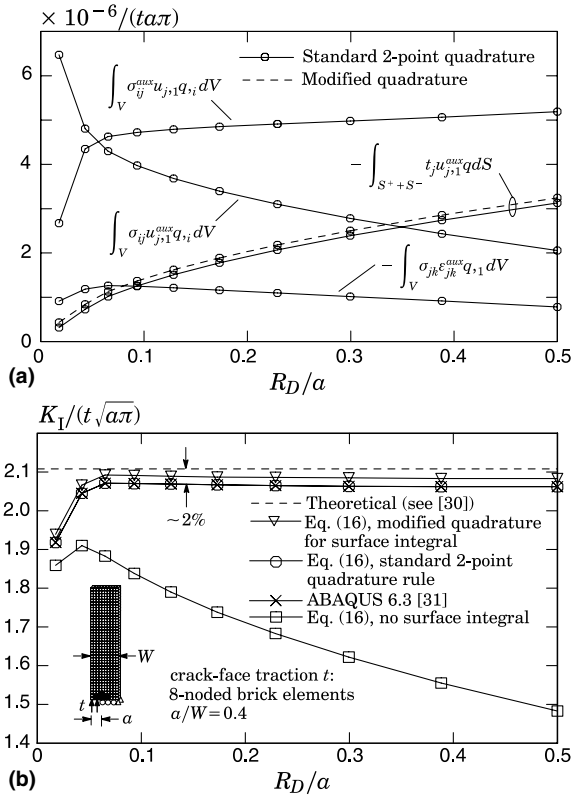

Fig. 6. (a) Normalized terms of the interaction integral vs. normalized domain size for the SE(T) specimen loaded by crack-face tractions. (b) Normalized stress intensity factors vs. domain size for the SE(T) specimen obtained using standard and modified quadrature for the surface integral, theoretical results and ABAQUS 6.3 [31].

quadrature. The lowest curve in Fig. 6(b) illustrates the impact of omitting the crack-face-traction contribution on the computed stress intensity factor values.

6. Curved cracks discretized by elements with piecewise-linear edges

Gosz et al. [18] and Kim et al. [16] compare stress intensity factors computed with and without the terms in the second integral of Eq. (16). Stress intensity factors computed by Gosz et al. [18] for a flat, elliptical crack embedded in an infinite homogeneous body under remote mode-I loading improve significantly when crack-front-curvature terms are included. Kim et al. [16] demonstrate an improvement in stress intensity factors when they employ the method of Gosz et al. [18] for a penny-shaped crack in a homogeneous cylinder loaded through remote displacements.

This section employs the interaction integral procedure described in Section 3 to compute mixed-mode stress intensity factors along penny-shaped and elliptical cracks in homogeneous solids. Meshes used for examples in this section have either linear or quadratic elements with *straight* edges along the crack front (often produced by mesh generation programs). For domain-integral computations, local crack-front curvature in the numerical model vanishes, and computations of r and θ values in local rectangular coordinates follow the descriptions in Section 4.2, Appendix B and Fig. 2(a) and (b). With this approach, gradients in

the auxiliary field due to curvilinear coordinates do not appear, and the second integral of Eq. (16) vanishes because it arises from the definition of 2-D auxiliary fields in a curvilinear coordinate system. This section explores the accuracy of this simplified approach for the computation of mixed-mode stress intensity factors.

6.1. Penny-shaped crack in an infinite solid under mixed-mode loading

Fig. 7 shows the problem of a circular crack in an infinite solid loaded by point forces above the crack plane. Kassir and Sih [32] provide analytical stress intensity factor solutions for this problem (see Appendix D.1), and the ABAQUS 6.3 benchmark manual contains mesh data and loading conditions which we use here. Fig. 8(a) shows a cross-section of the mesh obtained from the ABAQUS 6.3 input file, which defines 10,260 8-noded hexagonal elements. Boundary conditions consist of one fixed node at each end of the cylinder axis; nodal forces P and R in Fig. 7 act with magnitude 400 MN at distance 0.33 above the crack plane. Young's modulus and Poisson's ratio equal 200 GPa, and 0.3, respectively, and the ratio of cylinder height, H, and diameter, D, to crack radius, a, are $H/a = D/a = 80$. Fig. 8(b) shows domains of 24 radial sectors that discretize the crack front. Elements of size $L_e/a = 0.00129$ having one collapsed face surround the crack front, and the largest domain on which we compute values (domain five) has dimension $R_D/a = 0.04$. Thirty sectors discretize the cylinder in the radial direction about the z-axis, and we report stress intensity factors computed at element corner nodes on the crack front.

At each crack-front location, an average of the interaction integral values obtained from domains two through five yields stress intensity factors normalized as

$$K_n = \frac{Ka^{3/2}}{P\sqrt{\pi}}. \tag{25}$$

Fig. 9(a) shows normalized stress intensity factors along one-half of the crack front, obtained from present computations and from the analytical solutions listed in Appendix D.1. Stress intensity factors generated by

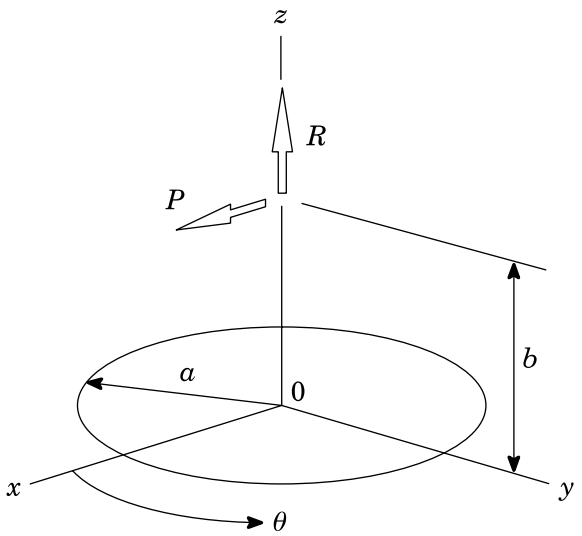

Fig. 7. (after Kassir and Sih, 1975) A penny-shaped crack in an infinite homogeneous solid loaded by point forces P and R acting at point $x = 0$, $y = 0$, $z = b$, and directed parallel to the x and z axes, respectively. For the ABAQUS 6.3 [31] benchmark model, $P = R = 400.0 \times 10^6$, and $b = 0.33$.

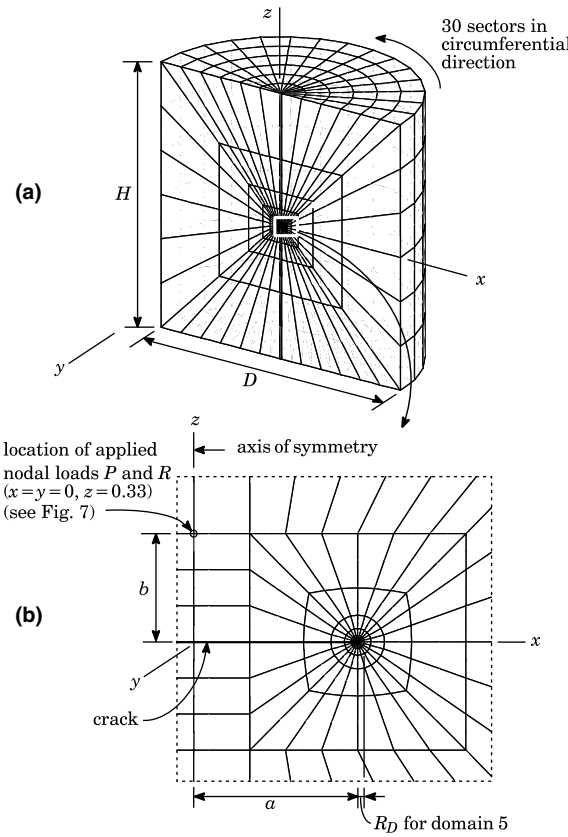

Fig. 8. (a) Section view of cylindrical mesh representing an infinite body with an embedded penny-shaped crack (from ABAQUS 6.3 benchmark library [31]). Dimension ratios are $H/a = D/a = 80$. (b) View of mesh discretization in crack-front region. Seven cylindrical domains with 24 sectors surround the crack front. For domain 1, $L_e/a = R_D/a = 0.00129$. For domain 5, $R_D/a = 0.04$.

the ABAQUS 6.3 interaction integral routines match current values for this case and do not appear in the figure. We also examine stress intensity factors obtained using the mesh shown in Fig. 8(a) following conversion to 20-noded hexagonal elements. Here again, element edges are straight, and thus local crack-front curvature is zero. Computations employ reduced $2 \times 2 \times 2$ integration and collapsed elements with quarter-point nodes incident on the crack front. Fig. 9(a) shows the variation in stress intensity factors obtained using the higher-order elements.

Fig. 9(b) compares energy release rate values generated using the interaction integral, the J-integral formulation described by Eq. (2), and the analytical solutions contained in Appendix D.1. Eq. (19) converts stress intensity factors to equivalent J-values. Normalization of J-integral values shown in Fig. 9(b) follows:

$$J_n = \frac{JEa^3}{P^2}. \tag{26}$$

The mesh of 20-noded elements leads to improved accuracy. This figure demonstrates that the accuracy of interaction integral computations along a curved crack front using a model with zero local curvature matches the high accuracy of J-integral computations which here do not include effects from crack-front curvature. Close agreement between results computed using the interaction integral, the J-integral, and analytical expressions indicates that excellent accuracy for this problem may be achieved by measuring r and θ from straight element edges as described in Section 4.2.

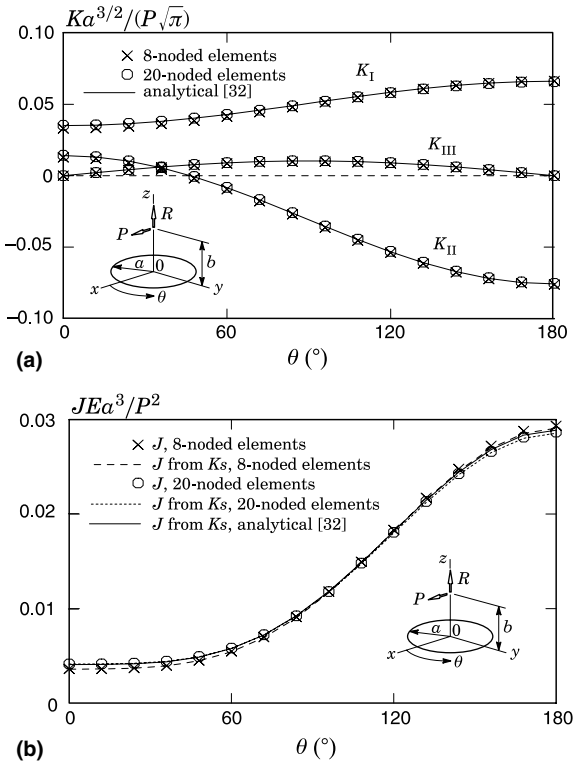

Fig. 9. (a) Normalized stress intensity factor values along the front of a penny-shaped crack under mixed-mode loading due to point forces P and R. (b) Normalized values of energy release rate determined from the J-integral, interaction integral values and analytical solutions.

6.2. An infinite solid with a flat elliptical crack under tension

Curvature effects may be more significant for elliptical cracks than for penny-shaped cracks. In this section, the computation of mode-I stress intensity factors along the front of a flat elliptical crack in a homogeneous solid supports a comparison between interaction integral results by Gosz et al. [18], J-integral results, and analytical values. Crack-face pressure provides loading conditions for the present analysis, giving additional insight into the influence of the surface-traction integral in Eq. (17). This example, and the corresponding problem in Gosz et al. [18], employ linear, 8-noded hexagonal elements. Gosz et al. [18] compute r and θ from an *analytically*-defined curve that describes the crack front; and thus include auxiliary field terms reflecting local curvilinear coordinates that appear in the second integral of Eq. (16). Here, computations of r and θ values use local orthogonal coordinates as described in Section 4.2 with crack front geometry defined by the element mesh.

The large rectangular specimen contains an embedded elliptical crack. The crack has a semi-minor-axis to semi-major-axis ratio of $a/c = 0.4$. To allow for arbitrary crack-face tractions, a full mesh is used here and consists of 26,504 8-noded brick elements. Fig. 10(a) shows one eighth of this mesh of size $L/c = 10$. Along the crack front shown in Fig. 10(b), evaluation of the interaction integral occurs over domains including elements incident on corner nodes along the crack front. Elements with collapsed faces surround the crack front, and have dimension $L_e/a = 0.0165$. Ten sectors and seven rings of elements discretize the region surrounding the crack. Here, we report the average of stress intensity factors computed using domains two through five at each crack front location.

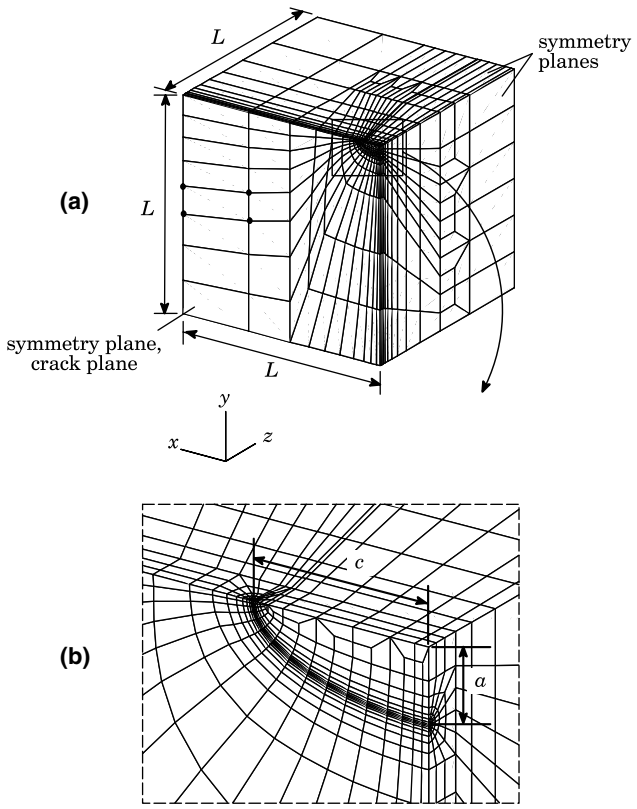

Fig. 10. (a) One eighth of the mesh defined to model a planar, elliptical crack in an infinite solid. Loading includes crack-face pressure and crack-face shear. The full mesh includes 26,504 8-noded brick elements. (b) View of mesh in crack-front region, where 7 rings divided into 20 sectors surround the crack front. Ratios $L/c = 10$, and $a/c = 0.4$.

Irwin [33] derives an analytical expression for the mode-I stress intensity factor along the front of an elliptical crack in an infinite solid under tension:

$$K_{\mathrm{I}} = \sigma_0 \sqrt{\frac{\pi}{Q}} \left(\frac{a}{c}\right) \left(a^2 \cos^2\phi + c^2 \sin^2\phi\right)^{1/2}, \tag{27}$$

where σ_0 is the remote uniform tensile stress, $2c$ and $2a$ are the major and minor axis lengths of the ellipse, parametric angle ϕ defines the crack-front location as described in Fig. 11, and $\sqrt{Q}$ is a complete elliptic integral of the second kind equal to $\ell/4c$, where ℓ is the arc length of the ellipse. Merkle [34] discusses a commonly-used approximate expression for Q, which for $a/c \leqslant 1$ is [30]

$$Q = 1 + 1.464 \left(\frac{a}{c}\right)^{1.65}. \tag{28}$$

The standard normalization of stress intensity factors for elliptical cracks follows:

$$K_{\mathrm{I}n} = \frac{K_{\mathrm{I}}}{S\sqrt{\frac{\pi a}{Q}}}, \tag{29}$$

where $S = \sigma_0$ for tension loading.

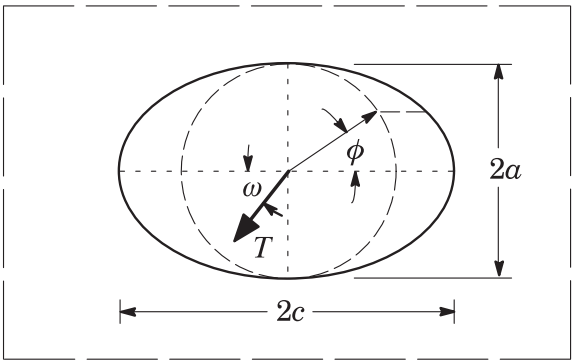

Fig. 11. Description of parametric angle ϕ, on an elliptical crack front where $a/c \leqslant 1.0$. Angle ω describes the direction of crack-face shear loading, represented by T.

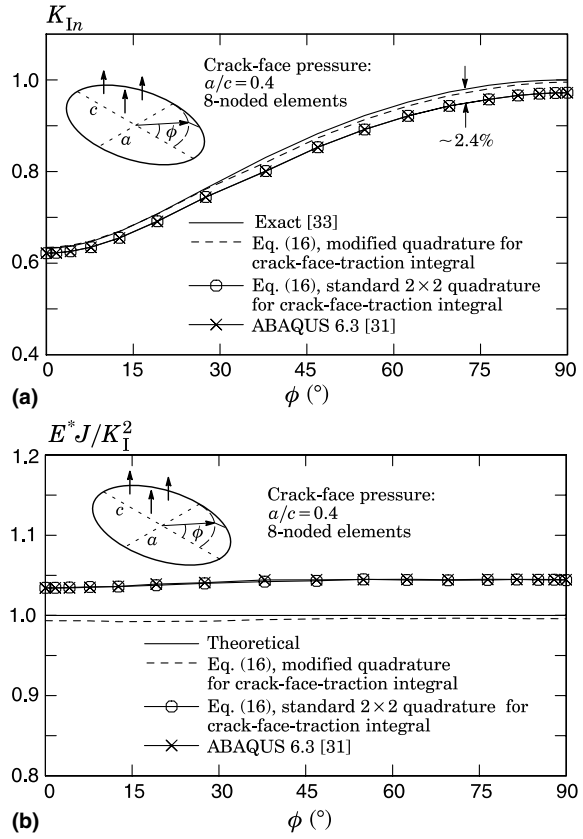

Fig. 12. (a) Comparison of numerical and analytical mode-I stress intensity factors along a flat elliptical crack loaded by crack-surface pressure in an infinite solid. (b) Comparison of J-integral values with energy release-rate values computed from interaction integral.

Fig. 12(a) shows the normalized mode-I stress intensity factors obtained from Eqs. (16) and (27) for crack-face pressure loading. With exact integration of the crack-face traction integral over the element incident on the crack front, the numerical result at all crack-front locations agrees to within 1% of the

analytical expression. With standard Gauss quadrature evaluation of Eq. (17), results are within 2.5% of theoretical values, and agree very closely with values generated by ABAQUS 6.3 [31]. Numerical results are accurate even along the more highly-curved portion of the crack front, whereas better path-independence of stress intensity factors occurs in areas of smaller curvature.

Fig. 12(b) compares K_I-values computed with the interaction integral to J-values computed using Eq. (2). Excellent agreement exists between interaction integral and J-integral values. Here, J-integral computations do not involve curvilinear coordinates as in Fernlund et al. [21]. Excellent overall accuracy and good correspondence between J-integral and interaction integral results for this problem imply that the use of straight-edged elements to discretize curved cracks essentially eliminates the influence of local crack-front curvature on interaction integral computations. Straight element edges enable simple computations of r and θ from local orthogonal coordinate systems, eliminate auxiliary-field gradients that arise due to curvilinear coordinates, and cause the second integral in Eq. (16) to vanish. Results in Fig. 12(a) and (b) demonstrate the accuracy that can be achieved through this approach, and an additional example further illustrates its usefulness for mixed-mode loading cases.

6.3. An infinite solid with a flat elliptical crack under shear

Application of tractions parallel to the faces of the elliptical crack described in Section 6.2 generates mode-II and mode-III loading. Computed stress intensity factors verify the accuracy of interaction integral

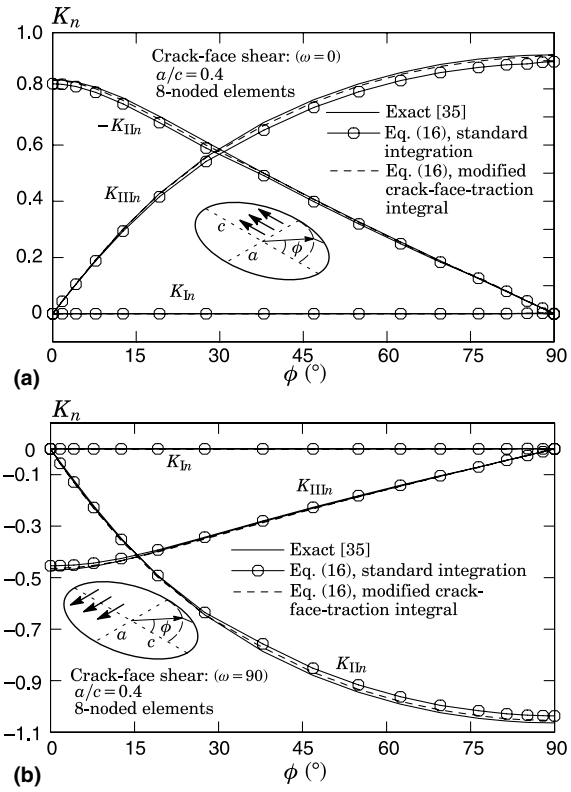

Fig. 13. Normalized analytical and numerical stress intensity factor values along the front of a flat elliptical carrying crack-face shear in an infinite solid. Crack-face shear induces loading in modes II and III for (a) shear parallel to the major axis ($\omega = 0$); (b) shear parallel to the minor axis ($\omega = 90$).

procedures for mixed-mode loading of a curved crack modeled with straight finite elements along the front. Evaluation of the interaction integral at each crack-front location again leads to reported values obtained from the average of domains 2–5.

Kassir and Sih [35] derive analytical expressions for stress intensity factors along the front of elliptical cracks under uniform shear loading, included here in Appendix D.2 for convenience. Fig. 11 illustrates the orientation of crack-face shear according to angle ω. At the ends of the major axis, mode-II stress intensity factors vary most rapidly for $\omega = 0$, and mode-III stress intensity factors vary most rapidly when $\omega = 90°$. We therefore examine stress intensity factors for these two cases.

Fig. 13(a) and (b) shows the variation of normalized stress intensity factors along the crack front from $\phi = 0$ to $\phi = 90°$. Normalization of the stress intensity factors follows Eq. (29), where S equals the magnitude of the uniform shear stress. Stress intensity factors show a maximum deviation of approximately 2.5% from theoretical values for standard quadrature evaluation of the crack-face traction integral over the elements incident on the crack front. Exact integration over these elements improves significantly the accuracy of stress intensity factors. This example demonstrates again that the interaction integral can yield very accurate results for curved cracks with zero local curvature in the model when the computation of r and θ values refers to local orthogonal coordinates. We now examine interaction integral results computed for curved cracks with non-zero local curvature in the model.

7. Analysis of cracks modeled with curved elements along front

When elements with curved edges discretize the crack front, non-zero local curvature in the model requires the use of curvilinear coordinates to compute accurate values of r and θ to evaluate the auxiliary fields. In these cases, the second integral of Eq. (16) is non-zero, and the gradients of some auxiliary fields involve terms that reflect explicitly the local curvature of the crack front [18]. This section examines the accuracy of stress intensity factors computed after omitting curvature terms during computation of the interaction integrals.

7.1. An infinite solid with a flat penny-shaped crack under tension

A cylindrical mesh with a penny-shaped crack under tension represents a standard problem to explore the influence of crack-curvature terms on the interaction integral. Fig. 14(a) shows the cross section of a mesh composed of 16,480 20-noded brick elements. A Young's modulus of 30,000 and Poisson's ratio of 0.3 describe material properties. The ratios of mesh height H and diameter D to crack radius a are $H/a = D/a = 80$. This cylindrical mesh has 20 sectors of elements surrounding the axis of symmetry, and domains surrounding the crack front are divided into 24 sectors, as seen in Fig. 14(b). Elements surrounding the crack front have a size of $L_e/a = 0.00129$ with one collapsed face and quarter-point nodes on edges normal to the front. Two models following the above description provide insight into the difference between stress intensity factors generated using a mesh with straight and curved elements incident on the crack front. For the mesh with straight edges, computations of r and θ in this section follow the procedure described in Appendix B which uses local orthogonal coordinates. For the mesh with curved elements, computations of r and θ use curvilinear coordinates along the analytically-defined curve representing the crack front.

Uniform crack-face pressure σ_0 imposes mode-I loading, and stress intensity factors computed at each crack-front location lead to reported stress intensity factor values obtained by averaging values from domains two through five. Normalization of stress intensity factors follows as:

$$K_{In} = \frac{K_I}{\sigma_0\sqrt{\pi a}}. \tag{30}$$

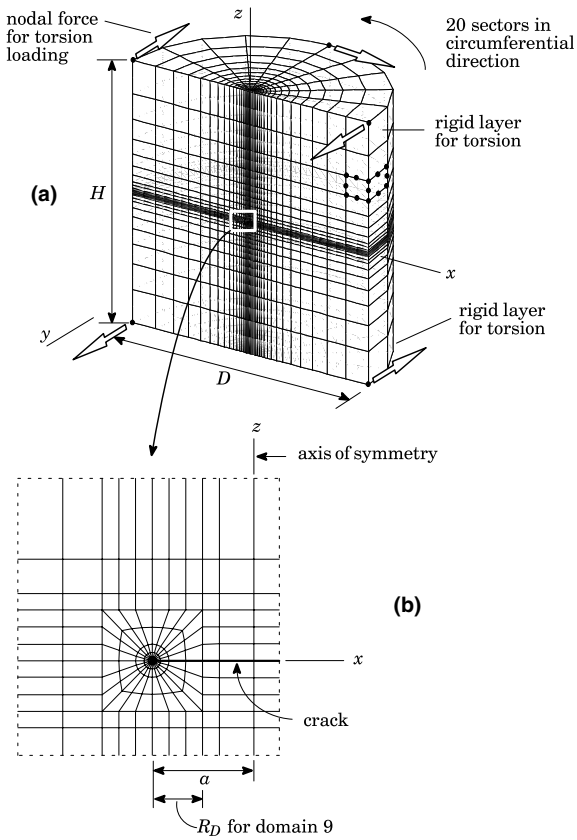

Fig. 14. (a) Section view of cylindrical mesh representing an infinite body with a penny-shaped crack. 16,480 20-noded hexagonal elements comprise the mesh. Dimensions are $H/a = D/a = 80$. (b) View of mesh in crack-front region.

Table 2 shows very good agreement among stress intensity factors obtained using the interaction integral in Eq. (16), the standard J-integral (Eqs. (2), (19)), analytical solutions for an infinite body, and asymptotic expressions for a finite cylinder. The asymptotic expression for stress intensity factors corresponds to a penny-shaped crack of radius a in a finite homogeneous cylinder of radius $b = D/2$ loaded in tension. The asymptotic solution is [36]

$$K_{\mathrm{I}} = \frac{2N\sqrt{a(1-a/b)}}{\pi^{3/2}(b^2-a^2)}\left(1+\frac{1}{2}\frac{a}{b}-\frac{5}{8}\frac{a^2}{b^2}+0.421\frac{a^3}{b^3}\right), \tag{31}$$

where N is the normal force acting on the cylinder. When the crack size shrinks to zero, i.e. $a/b \to 0$, this expression reduces to the stress intensity factor for a penny-shaped crack in an infinite body under tension [32]

$$K_{\mathrm{I}} = \frac{2}{\pi}\sigma_0\sqrt{\pi a}, \tag{32}$$

where σ_0 is the remote tensile stress, equal to $N/\pi b^2$ for the finite cylinder, or the crack-face-opening pressure for an infinite cylinder.

The mesh with curved elements yields more accurate interaction integral and J-integral results than the mesh with straight-edged elements. The straight-edge mesh includes zero error from the crack-face traction integral, while the value from the mesh with curved edges includes some error due to the inexact 4×4 quadrature employed to integrate Eq. (17). A comparison of numerical results generated from the two meshes

Table 2
Normalized stress intensity factors for a penny-shaped crack in an infinite homogeneous solid under torsion and tension, illustrated in Figs. 3 and 14

Loading	Source	Result	% Difference
Tension K_{In}	Infinite body [32]	0.6366	–
	Finite cylinder [36]	0.6366	0.00
	Interaction integral (straight edges)	0.6299	−1.05
	From *J*-integral (straight edges)	0.6309	−0.90
	Interaction integral (curved edges)	0.6316	−0.79
	From *J*-integral (curved edges)	0.6348	−0.28
Torsion K_{IIIn}	Infinite body [32]	0.4244	–
	Finite cylinder [36]	0.4244	0.00
	Interaction integral (straight edges)	0.4268	+0.57
	From *J*-integral (straight edges)	0.4307	+1.48
	Interaction integral (curved edges)	0.4194	−1.18
	From *J*-integral (curved edges)	0.4228	−0.38

Normalization follows $K_{In} = K_I(\sigma_0\sqrt{\pi a})$ for tension, and for torsion, $K_{III_n} = K_{III}/(\tau_0\sqrt{\pi a})$, where $\tau_0 = 2Ta/(\pi b^4)$.

indicates that the combined influence of the curvature terms in the auxiliary field and the second integral of Eq. (16) must be less than ≈1.0% for this problem.

7.2. An infinite solid with a flat penny-shaped crack under torsion

The meshes employed in Section 7.1 also enable computation of mode-III stress intensity factors for cracks in a homogeneous cylinder under torsion. Boundary conditions for torsion loading include nodal loads and one fixed node at each end of the cylinder (see Fig. 14(a)). Assignment of a high Young's modulus to the layer of elements at both ends of the cylinder ensures a uniform distribution of torsional stresses. Other regions of the mesh have a Young's modulus of 30,000 and a Poisson's ratio of 0.3. We again report stress intensity factor values obtained from the average of domains two through five.

Table 2 shows good agreement between stress intensity factors obtained from the interaction integral, the *J*-integral, analytical solutions for an infinite body and asymptotic expressions for a finite cylinder. An expression for the mode-III stress intensity factor along a penny-shaped crack of radius a, in a finite homogeneous cylinder of radius $b = D/2$, loaded in torsion is [36]

$$K_{III} = \frac{8Ta^{3/2}\sqrt{1-a/b}}{3\pi^{3/2}(b^4-a^4)}\left(1+\frac{1}{2}\frac{a}{b}+\frac{3}{8}\frac{a^2}{b^2}+\frac{5}{16}\frac{a^3}{b^3}-\frac{93}{128}\frac{a^4}{b^4}+0.038\frac{a^5}{b^5}\right), \tag{33}$$

where T is total torque. When the crack size shrinks to zero, i.e. $a/b \to 0$, this expression reduces to

$$K_{III} = \frac{4}{3\pi}\frac{2Ta}{\pi b^4}\sqrt{\pi a}. \tag{34}$$

For torque T applied to an uncracked cylinder of radius $b = D/2$, the quantity $\tau_0 = 2Ta/\pi b^4$ equals the magnitude of the linearly-varying shear stress, τ, at distance $r = a$ from the longitudinal axis. For the perturbed problem, in which loading conditions consist of crack-face tractions rather than far-field loads, $\tau = 2Tr/\pi b^4$ defines the linearly-varying shear tractions applied to the crack faces between $r = 0$ and $r = a$. For a linearly-varying traction applied on the crack face to generate torsional loading (magnitude τ_0 at a), the stress intensity factor for a penny-shaped crack in an infinite body is [32]

$$K_{III} = \frac{4}{3\pi}\tau_0\sqrt{\pi a}. \tag{35}$$

Normalization of K_{III} follows:

$$K_{IIIn} = \frac{K_{III}}{\tau_0\sqrt{\pi a}}. \tag{36}$$

As Table 2 shows, the stress intensity factor computed from the interaction integral is slightly more accurate when the model crack front has straight elements, but computations from the J-integral improve in accuracy for the mesh with curved front elements. The curvature terms omitted from the interaction integral may play a greater role for the torsion loading here than for the tension loading. Nevertheless, errors introduced by approximate evaluations of the interaction integral (that omit curvature terms) remain less than 2% for this example. This investigation gives an idea of the good accuracy that can be achieved using the simpler, standard expression, and lends support to investigations (e.g. [9]) that employ this approach.

8. Summary and conclusions

This work describes an interaction integral formulation and computational procedure applicable to compute mixed-mode, stress intensity factors for curved, planar 3-D cracks in homogeneous solids under remote mechanical loading and applied crack-face tractions. The described procedures adapt readily into existing 3-D codes that utilize a domain-integral formulation to compute J-integral values. The commonly adopted, 2-D Williams solutions for the mixed-mode, auxiliary field in the interaction integral does not satisfy equilibrium or strain–displacement compatibility when expressed in curvilinear coordinates used for curved crack fronts, thereby leading to additional terms in the interaction integral. A potentially significant contribution to the interaction integral arises when the otherwise traction-free crack faces have applied loads. Through numerical solutions for several 3-D crack configurations, this work explores the significance of the additional (curvature) terms on computed stress intensity factors relative to the various techniques often employed to mesh the cracked geometry (linear *vs*. quadratic elements, straight vs. curved elements along the crack front). These examples also explore the significance on stress intensity factors of loadings (tractions) applied directly on the crack faces.

Evaluation of the interaction integral requires values for the auxiliary fields at integration points for elements within a domain defined at a crack-front location. The singular nature of the auxiliary fields at the crack front necessitates highly accurate values for the crack tip coordinates (r,θ) of the integration points—otherwise auxiliary field values become grossly incorrect. The use of straight or curved finite elements along the crack front dictates the choice of algorithms to compute the (r,θ) values. For curved front elements, an iterative Newton procedure, coupled with an analytical definition for the local crack-front geometry, is often adopted. We show here that such a procedure may introduce unacceptable errors for crack fronts modeled with straight elements, and thus describe an alternative procedure to compute accurate values for (r,θ) using a local, orthogonal coordinate system for each straight element incident on the crack front.

The use of elements with straight edges (linear or quadratic) along the crack front, coupled with the new procedure to compute (r,θ) values at integration points, eliminates the additional terms appearing in the interaction integral formulation for curvilinear coordinates. Numerical evaluation of the interaction integral becomes identical to that for an entirely straight crack front. The stress intensity factors computed here for models constructed with straight elements along curved crack fronts agree very closely with corresponding values obtained through the J-integral and with available analytical solutions. The use of quadratic elements (with straight edges) provides some additional increase in the solution quality compared to an identical mesh of linear elements.

The examples here using curved (quadratic) elements along the crack front omit terms in the interaction integral that arise from the definition of auxiliary fields in curvilinear coordinates. Comparisons of com-

puted stress intensity factors with corresponding J-integral values and with analytical solutions demonstrate that this simpler interaction integral method yields highly accurate values for curved cracks with reasonable levels of mesh refinement that also provide accurate J-values.

The curvature terms appearing in the interaction integral appear to have an effect similar to the use of higher-order interpolation functions (p-version mesh refinement). Higher-order elements may improve the accuracy of a solution for a boundary-value problem by representing more realistically the gradients in field quantities. Similarly, auxiliary-field terms that arise due to curvilinear coordinates represent a more accurate description along a curved crack, and thus improve interaction integral results. However, as normal mesh refinement reduces element size (h-version mesh refinement), linear elements represent accurately the gradients present in the actual fields, and the relative influence of curvature terms must diminish. The influence of curvature terms in the interaction integral may be significant in some meshes [18], but very small in others, as shown here. The analyses described here demonstrate that omission of auxiliary-field and interaction integral terms arising from crack-front curvature simplifies the computation of interaction integrals and yields accurate stress intensity factors with reasonable levels of mesh discretization.

Finally, the numerical examples demonstrate clearly the important contribution from the crack-face integral in models with traction-bearing crack faces. For good accuracy and path-independent stress intensity factors, the crack-face traction integral should be included. The exact integration procedure developed here for use with straight-sided crack-front elements provides a simple approach to increase the accuracy of computed stress intensity factors.

Acknowledgement

The authors are grateful for the support provided by the NASA Graduate Student Researchers Program (NGT 2-52271) and the NASA-Ames Engineering for Complex Systems Program (NAG 2-1424), for both of which NASA-Ames Chief Engineer Dr. Tina Panontin serves as the technical monitor. We also extend thanks to the National Science Foundation (NSF) Mechanics and Materials Program (CMS-0115954). The first author wishes to thank Mr. Alok Sutradhar for his helpful suggestions. Any opinions, findings, conclusions or recommendations expressed in this publication do not necessarily reflect the views of the sponsors.

Appendix A

A.1. Auxiliary fields

Auxiliary fields employed here follow the 2-D analytical solutions obtained by Williams [1] for asymptotic stresses and displacements near a crack tip [30]:

$$\sigma_{11}^{\text{aux}} = \frac{1}{\sqrt{2\pi r}}\left[K_{\text{I}}^{\text{aux}}\cos\frac{\theta}{2}\left(1-\sin\frac{\theta}{2}\sin\frac{3\theta}{2}\right) - K_{\text{II}}^{\text{aux}}\sin\frac{\theta}{2}\left(2+\cos\frac{\theta}{2}\cos\frac{3\theta}{2}\right)\right], \tag{A.1}$$

$$\sigma_{22}^{\text{aux}} = \frac{1}{\sqrt{2\pi r}}\left[K_{\text{I}}^{\text{aux}}\cos\frac{\theta}{2}\left(1+\sin\frac{\theta}{2}\sin\frac{3\theta}{2}\right) + K_{\text{II}}^{\text{aux}}\sin\frac{\theta}{2}\cos\frac{\theta}{2}\cos\frac{3\theta}{2}\right], \tag{A.2}$$

$$\sigma_{12}^{\text{aux}} = \frac{1}{\sqrt{2\pi r}}\left[K_{\text{I}}^{\text{aux}}\cos\frac{\theta}{2}\sin\frac{\theta}{2}\cos\frac{3\theta}{2} + K_{\text{II}}^{\text{aux}}\cos\frac{\theta}{2}\left(1-\sin\frac{\theta}{2}\sin\frac{3\theta}{2}\right)\right], \tag{A.3}$$

$$\sigma_{13}^{\text{aux}} = -\frac{K_{\text{III}}^{\text{aux}}}{\sqrt{2\pi r}}\sin\frac{\theta}{2}, \tag{A.4}$$

$$\sigma_{23}^{\text{aux}} = \frac{K_{\text{III}}^{\text{aux}}}{\sqrt{2\pi r}}\cos\frac{\theta}{2}, \tag{A.5}$$

$$\sigma_{33}^{\text{aux}} = \begin{cases} v(\sigma_{11}^{\text{aux}} + \sigma_{22}^{\text{aux}}) & \text{plane strain,} \\ 0 & \text{plane stress,} \end{cases} \tag{A.6}$$

$$u_1^{\text{aux}} = \frac{1}{2\mu}\sqrt{\frac{r}{2\pi}}\left[K_{\text{I}}^{\text{aux}}\cos\frac{\theta}{2}\left(\kappa - 1 + 2\sin^2\frac{\theta}{2}\right) + K_{\text{II}}^{\text{aux}}\sin\frac{\theta}{2}\left(\kappa + 1 + 2\cos^2\frac{\theta}{2}\right)\right], \tag{A.7}$$

$$u_2^{\text{aux}} = \frac{1}{2\mu}\sqrt{\frac{r}{2\pi}}\left[K_{\text{I}}^{\text{aux}}\sin\frac{\theta}{2}\left(\kappa + 1 - 2\cos^2\frac{\theta}{2}\right) - K_{\text{II}}^{\text{aux}}\cos\frac{\theta}{2}\left(\kappa - 1 - 2\sin^2\frac{\theta}{2}\right)\right], \tag{A.8}$$

$$u_3^{\text{aux}} = \frac{K_{\text{III}}^{\text{aux}}}{\mu}\sqrt{\frac{2r}{\pi}}\sin\frac{\theta}{2}, \tag{A.9}$$

where v and μ are, respectively, Poisson's ratio and the shear modulus, and

$$\kappa = \begin{cases} 3 - 4v & \text{plane strain} \\ \frac{3-v}{1+v} & \text{plane strain.} \end{cases} \tag{A.10}$$

Appendix B

B.1. Computation of r and θ for crack fronts with straight element edges

The following steps describe one procedure to compute r and θ for curved, planar crack fronts defined by elements with straight edges. Definitions use coordinates in the local crack front coordinate system shown in Fig. 1, and the notation described in Fig. 2(a) and (b):

(1) Determine the crack-front segment nearest the integration point, and obtain coordinates of the nodes at each end of the segment. Call these points A and B, where B has the larger value of X_3.
(2) Use element shape functions to determine the coordinates of the integration point P in the local crack-front system, (X_1^p, X_2^p, X_3^p)

$$X_i^p = \sum_{I=1}^{n} N_I (X_i)_I. \tag{B.1}$$

(3) The area of the parallelogram defined by AB and AP equals the magnitude of the cross product of AB and AP, or $\|AB \times AP\|$. Compute height r of the parallelogram as the area divided by the length of the base AB:

$$r = \frac{\|AB \times AP\|}{\|AB\|}. \tag{B.2}$$

Point C is the projection of integration point P onto the crack plane, which is the X_1–X_3 plane. In local coordinates, $C = (X_1^p, 0, X_3^p)$. Point D is the point on segment AB closest to point C. Angle

PDC defines θ. The plane *PDC* on which r is defined, coincides with the local X_1–X_2 plane only for straight crack fronts. Fig. 2(b) illustrates quadrants of a coordinate system in the plane defined by points *PDC*, with point *D* at the origin, and segment *DC* orthogonal to the local X_2-axis. Computation of θ involves two additional steps:

(4) Use X_2^p to determine if *P* lies above or below the crack plane, and use the sign of cross product $AB \times AC$ to determine whether the integration point is ahead of or behind segment *AB*.

(5) For quadrants I–IV illustrated in Fig. 2(b), compute θ as

$$\text{I: } \theta = \sin^{-1}\left(\frac{X_2^p}{r}\right); \quad \text{II: } \theta = 180^\circ - \sin^{-1}\left(\frac{X_2^P}{r}\right), \tag{B.3}$$

$$\text{III: } \theta = -180^\circ - \sin^{-1}\left(\frac{X_2^P}{r}\right); \quad \text{IV: } \theta = \sin^{-1}\left(\frac{X_2^P}{r}\right). \tag{B.4}$$

For the crack-face-traction integral where $\theta = \pm\pi$, the sign of the X_2-coordinate of the centroid of the loaded element conveniently indicates the sign of θ.

Appendix C

C.1. Exact integration of crack-face-traction integral for elements incident on the crack front having straight edges

A change of variables permits the exact integration of Eq. (17). For a 1-D function $f(r)$ with an inverse square-root singularity at one boundary of the domain of integration, the substitution of $t = \sqrt{r}$, removes the singularity [37]

$$\int_a^b f(r)\mathrm{d}r = \int_0^{\sqrt{b-a}} 2tf(t^2+a)\mathrm{d}t \quad (b > a). \tag{C.1}$$

For example, define $f(r) = 1/\sqrt{r}$, and assign integration limits a and b as $r = 0$ and $r = L_e$, the length of an element adjacent to the crack front, illustrated in Fig. 4(d). The relationship $t^2 = r$ leads to $f(t^2 + a) = 1/t$, giving

$$\int_0^{L_e} \frac{1}{\sqrt{r}}\,\mathrm{d}r = \int_0^{\sqrt{L_e}} 2t\frac{1}{t}\mathrm{d}t = \int_0^{\sqrt{L_e}} 2\,\mathrm{d}t = 2\sqrt{L_e}, \tag{C.2}$$

which is the exact result. To evaluate Eq. (17) over a flat 2-D surface where coordinate z is tangent to the crack front, $f(z,r)$ includes traction values, t_j, auxiliary-displacement derivatives, $u_{j,1}^{\mathrm{aux}}$, and q-function values. Standard Gauss quadrature is adequate to integrate exactly in the z-direction.

To implement the above procedure numerically, a change of variables in parent (natural, intrinsic) coordinates is performed. From (C.1), we have

$$\int_{-1}^{1}\int_{-1}^{1} f(\xi,\eta)\mathrm{d}\eta\,\mathrm{d}\xi = \int_{-1}^{1}\int_{0}^{\sqrt{2}} 2tf(\xi,t^2-1)\mathrm{d}t\,\mathrm{d}\xi, \tag{C.3}$$

where the inverse square-root singularity of $f(\xi,\eta)$ in parent coordinates corresponds to the lower integration boundary $\eta = -1$. In Eq. (C.3) and in the steps that follow, we assume that parent coordinate ξ is tangent to the crack front, and that η corresponds to distance r from the crack front. Integrands in Eq. (C.3) include traction values, t_j, auxiliary-displacement derivatives, $u_{j,1}^{\mathrm{aux}}$, q-function values, and the determinant of the coordinate Jacobian, $\det\mathbf{J}$.

In order to apply a Gauss quadrature rule formulated for the interval $[-1,1]$, to the inner integral of Eq. (C.3) over interval $[0,\sqrt{2}]$, it is necessary to employ the standard transformation [28]

$$t = \frac{b-a}{2}\eta + \frac{b+a}{2}, \tag{C.4}$$

where a and b are the new limits of integration, 0 and $\sqrt{2}$, respectively. Eq. (C.4) gives

$$t = \frac{1}{\sqrt{2}}(\eta+1) \quad \text{and} \quad \frac{\mathrm{d}t}{\mathrm{d}\eta} = \frac{1}{\sqrt{2}}, \tag{C.5}$$

and the quadrature for Eq. (C.3) over one element face becomes

$$\frac{1}{\sqrt{2}}\sum_{p}^{\text{gpts}} 2tf(\xi, t^2-1)w_p, \tag{C.6}$$

where the summation includes all Gauss integration points at parent coordinates (ξ,t), where Eq. (C.5) defines t. Weights w_p in Eq. (C.6) correspond to the standard Gauss-quadrature rule formulated over interval $\xi = \eta = [-1,1]$, and $1/\sqrt{2}$ is the Jacobian of the interval transformation, or $\mathrm{d}t/\mathrm{d}\eta$ in (C.5).

The following steps describe the procedure for evaluating Eq. (17) through the quadrature described by Eq. (C.6).

(1) Collect data for element faces and nodes (coordinates, q-values, tractions etc.).
(2) Loop over integration points. A 2×2 quadrature rule yields exact results for the constant face tractions employed in this study.
(3) For the current integration point, obtain weight w_p, and parent coordinates (ξ,η) based on a standard rule for the interval $\xi = \eta = [-1,1]$.
(4) Shift the value of η according to Eq. (C.5): $\eta_{\text{new}} = t = 1/\sqrt{2}(\eta+1)$.
(5) Redefine η as in Eq. (C.3): $\eta = (\eta_{\text{new}})^2 - 1$.
(6) Evaluate standard element shape functions, shape-function derivatives, the coordinate Jacobian matrix, and the determinant of the coordinate Jacobian matrix, $\det \mathbf{J}$, using the standard value for ξ, and the value of η obtained from step 5.
(7) Use element shape functions to determine the local coordinates, (X_1^p, X_2^p, X_3^p), of the current integration point, and the q-value and traction value at the integration point.
(8) Compute distance r and angle $\theta = \pm\pi$ from the crack front to the integration point based on the coordinates determined in step 7.
(9) Evaluate the auxiliary-displacement derivative $u_{j,1}^{\text{aux}}$ using μ, r and θ from the previous step, and 1.0 for the stress intensity factor.
(10) Evaluate the integrand in Eq. (C.6) as: $w_p \times q(\xi,\eta) \times t_j(\xi,\eta) \times u_{j,1}^{\text{aux}}(\xi,\eta) \times \det \mathbf{J}$, where summation is implied by the repeated index, and η follows from step 5.
(11) Complete the quadrature in Eq. (C.6) by multiplying the result of step 10 by $1/\sqrt{2} \times 2\eta_{\text{new}}$.
(12) Sum contribution from integration point, and cycle to next point.

In steps 1–12, only steps 4, 5 and 11 differ from standard quadrature procedures. Examples in Sections 5 and 6 demonstrate that including these three simple steps to integrate Eq. (17) exactly, may markedly improve the accuracy of stress intensity factors. Steps 4, 5 and 11 are required for the exact integration of Eq. (17) for 8-noded elements with four nodes on each face, and for 20-noded elements with 8 nodes on each face. When quarter-point elements border the crack front, steps 4, 5 and 11 should not be employed because the quarter-point nodes cause standard quadrature to integrate Eq. (17) exactly. Standard Gauss quadrature provides good accuracy for elements not incident on the crack front.

Appendix D

D.1. Stress intensity factors for a penny-shaped crack loaded by point forces

Kassir and Sih [32] provide analytical solutions for the stress intensity factors around a penny-shaped crack in an infinite homogeneous medium loaded by point forces above the crack plane. Fig. 7 illustrates the geometry and nomenclature used in the following expressions. For point-load P, which acts parallel to the x-axis at distance b from the crack plane, the stress intensity factors are

$$K_{\mathrm{I}} = \frac{P\cos\theta}{4\pi^{3/2}(1-\nu)a^{3/2}}\left[(1-2\nu)\left(\cot^{-1}z_0 - \frac{z_0}{(1+z_0^2)}\right) - \frac{2z_0}{(1+z_0^2)^2}\right], \tag{D.1}$$

$$K_{\mathrm{II}} = \frac{P\cos\theta}{4\pi^{3/2}(1-\nu)(2-\nu)a^{3/2}}\left\{3(1-\nu)(1-2\nu)z_0\left[\cot^{-1}z_0 - \frac{z_0}{1+z_0^2}\right] + \frac{2}{1+z_0^2}\left[2(1-\nu^2) - \frac{(2-\nu)z_0^2}{1+z_0^2}\right]\right\}, \tag{D.2}$$

$$K_{\mathrm{III}} = \frac{(1-2\nu)P\sin\theta}{4\pi^{3/2}(2-\nu)a^{3/2}}\left[3 - 3z_0\cot^{-1}z_0 + \frac{1}{1+z_0^2}\right], \tag{D.3}$$

where constant $z_0 = b/a$. Here, the sign of Eq. (D.3) agrees with the definition of auxiliary displacement u_3 (Eq. (A.9)), as defined in the crack-front coordinate system shown in Fig. 1. For point force R, which acts parallel to the z-axis at distance b from the crack plane, the stress intensity factors are

$$K_{\mathrm{I}} = -\frac{R}{2\pi^{3/2}(1-\nu)a^{3/2}}\left(\frac{1}{1+z_0^2}\right)\left[1-\nu+\frac{z_0^2}{1+z_0^2}\right], \tag{D.4}$$

$$K_{\mathrm{II}} = \frac{R}{4\pi^{3/2}(1-\nu)a^{3/2}}\left\{(1-2\nu)\left[\frac{z_0}{1+z_0^2} - \cot^{-1}z_0\right] - \frac{2z_0}{(1+z_0^2)^2}\right\}, \tag{D.5}$$

$$K_{\mathrm{III}} = 0. \tag{D.6}$$

D.2. Stress intensity factors for an elliptical crack under shear in an infinite body

Kassir and Sih [35] obtain expressions for mode-II and mode-III stress intensity factors along the front of a shear-loaded, flat elliptical crack in a homogeneous solid. Fig. 11 illustrates the measurement of crack-front location ϕ, and the orientation ω of shear loading with respect to the axes of the ellipse. Expressions for the mode-II and mode-III stress intensity factors at location ϕ, are [35]

$$K_{\mathrm{II}} = -\frac{4\mu}{(ca)^{3/2}}\left(a^2\sin^2\phi + b^2\cos^2\phi\right)^{-1/4}(cB\sin\phi + aA\cos\phi), \tag{D.7}$$

$$K_{\mathrm{III}} = \frac{4\mu(1-\nu)}{(ca)^{3/2}}\left(a^2\sin^2\phi + b^2\cos^2\phi\right)^{-1/4}(cA\sin\phi - aB\cos\phi), \tag{D.8}$$

where μ is the shear modulus, and quantities A and B equal

$$A = \frac{ca^2k^2T\cos\omega}{4\mu\left[(k^2-\nu)E(k) + \nu k'^2K(k)\right]}, \tag{D.9}$$

$$B = \frac{ca^2k^2T\sin\omega}{4\mu\left[\left(k^2+\nu k'^2\right)E(k)-\nu k'^2K(k)\right]}, \tag{D.10}$$

where

$$k^2 = 1-\left(\frac{a}{c}\right)^2 \quad \text{and} \quad k^2+k'^2 = 1. \tag{D.11}$$

Solutions to complete elliptical integrals of the first and second kinds, represented, respectively, by $E(k)$ and $K(k)$, are available through many commercial mathematical software packages, and are tabularized in standard references such as Abramowitz and Stegun [38].

References

[1] Williams ML. On the stress distribution at the base of a stationary crack. ASME J Appl Mech 1957;24:109–14.
[2] Rice JR. A path independent integral and the approximate analysis of strain concentration by notches and cracks. J Appl Mech 1968;35:379–86.
[3] Chen FHK, Shield RT. Conservation laws in elasticity of the *J*-integral type. J Appl Math Phys (ZAMP) 1977;28:1–22.
[4] Shih CF, Moran B, Nakamura T. Energy release rate along a three-dimensional crack front in a thermally stressed body. Int J Fract 1986;30:79–102.
[5] Yau JF, Wang SS, Corten HT. A mixed-mode crack analysis of isotropic solids using conservation laws of elasticity. ASME J Appl Mech 1980;47:335–41.
[6] Nakamura T, Parks DM. Antisymmetrical 3-D stress field near the crack front of a thin elastic plate. Int J Solids Struct 1989;25:1411–26.
[7] Shih CF, Asaro RJ. Elastic–plastic analysis of cracks on bimaterial interfaces: part I—small scale yielding. ASME J Appl Mech 1988;55:299–316.
[8] Dhondt G. On corner point singularities along a quarter circular crack subject to shear loading. Int J Fract 1998;89:L33–8.
[9] Krysl P, Belytschko T. The element free Galerkin method for dynamic propagation of arbitrary 3-D cracks. Int J Numer Methods Engng 1999;44:767–800.
[10] Nakamura T, Parks DM. Determination of elastic *T*-stress along three-dimensional crack fronts using an interaction integral. Int J Solids Struct 1992;29:1597–611.
[11] Cho YJ, Beom HG, Earmme YY. Application of a conservation integral to an interface crack interacting with singularities. Int J Fract 1994;65:63–73.
[12] Stern M, Becker EB, Dunham RS. A contour integral computation of mixed-mode stress intensity factors. Int J Fract 1976;12:359–68.
[13] Knowles JK, Sternberg E. On a class of conservation laws in linearized and finite elastostatics. ArchRat Mechanics Ana 1972;7:55–129.
[14] Im S, Kim K-S. An application of two-state *M*-integral for computing the intensity of the singular near-tip field for a generic wedge. J Mech Phys Solids 2000;48:129–51.
[15] Choi NY, Earmme YY. Evaluation of stress intensity factors in a circular arc-shaped interfacial crack using *L*-integral. Mech Materials 1992;14:141–53.
[16] Kim YJ, Kim H-G, Im S. Mode decomposition of three-dimensional mixed-mode cracks via two-state integrals. Int J Solids Struct 2001;38:6405–26.
[17] Nahta R, Moran B. Domain integrals for axisymmetric interface problems. Int J Solids Struct 1993;30:2027–40.
[18] Gosz M, Dolbow J, Moran B. Domain integral formulation for stress intensity factor computation along curved three-dimensional interface cracks. Int J Solids Struct 1998;35:1763–83.
[19] Gosz M, Moran B. An interaction energy integral method for computation of mixed-mode stress intensity factors along non-planar crack fronts in three dimensions. Engng Fract Mech 2002;69:299–319.
[20] Lee Y, Im S. On the computation of the near-tip stress intensities for three-dimensional wedges via two-state *M*-integral. J Mech Phys Solids 2003;51:825–50.
[21] Fernlund G, McCammond D, Spelt JK. Curvilinear formulation of the 3-D *J* integral: Application to delamination cracking of curved laminates. Compos Struct 1994;28:123–30.
[22] Eriksson K. A domain independent integral expression for the crack extension force of a curved crack in three dimensions. J Mech Phys Solids 2002;50:381–403.
[23] Dolbow J, Gosz M. On the computation of mixed-mode stress intensity factors in functionally graded materials. Int J Solids Struct 2002;39:2557–74.

[24] Kim J-H, Paulino GH. A new approach to compute *T*-stress in functionally graded materials by means of the interaction integral method. Engng Fract Mech 2004;71:1907–50.
[25] Anderson TL. Fracture Mechanics, Fundamentals and Applications. 2nd ed. New York: CRC Press; 1995.
[26] Gullerud AS, Koppenhoefer KC, Roy A, RoyChowdhury S, Walters MC, Dodds Jr RH. WARP3D–release 15 manual. Report No. UILU-ENG-95-2012, Civil Engineering, University of Illinois, Urbana, IL 61801, USA, 2004.
[27] Cook RD, Malkus DS, Plesha ME, Witt RJ. Concepts and Applications of Finite Element Analysis. New York: John Wiley & Sons; 2002.
[28] Evans G. Practical Numerical Integration. Chichester: John Wiley and Sons; 1993.
[29] Nakamura T, Parks DM. Three-dimensional stress field near the crack front of a thin elastic plate. ASME J Appl Mech 1988;55:805–13.
[30] Anderson TL. Fracture Mechanics, Fundamentals and Applications. Second ed. New York: CRC Press; 1995.
[31] ABAQUS/Standard User's Manual, version 6.3, Hibbitt, Karlsson and Sorenson, Inc., Pawtucket, RI, 62860-4847, USA; 2002.
[32] Kassir MK, Sih GC. Mechanics of fracture 2, three-dimensional crack problems. Leyden: Noordhoff International Publishing; 1975.
[33] Irwin GR. The crack extension force for a part through crack in a plate. ASME J Appl Mech 1962;29:651–4.
[34] Merkle JG. A review of some of the existing stress intensity factor solutions for part-through surface cracks. ORNL-TM-3983, U.S. Atomic Energy Commission; 1973.
[35] Kassir MK, Sih GC. Three-dimensional stress distribution around an elliptical crack under arbitrary loadings. ASME J Appl Mech 1966;33:601–11.
[36] Benthem JP, Koiter WT. Asymptotic approximations to crack problems. In: Sih GC, editor. Mechanics of fracture 1, methods of analysis and solutions of crack problems. Leyden: Noordhoff International Publishing; 1973.
[37] Press WH, Teukolsky SA, Vetterling WT, Flannery BP. Numerical recipies in Fortran 77. Cambridge: Press Syndicate of the University of Cambridge; 2001.
[38] Abramowitz M, Stegun IA. Handbook of mathematical functions. New York: Dover Publications, Inc.; 1972.